

Comparative experimental and numerical study of the heat transfer from a heated wall to swirling impinging jets

by G. Paolillo*, C.S. Greco*, T. Astarita* and G. Cardone*

* Dept. of Industrial Engineering, University of Naples "Federico II", Piazzale Tecchio 80, 80125 Napoli, Italy, gennaro.cardone@unina.it

Abstract

This work presents a comparison of the results from an experimental and numerical investigation of impinging swirling jets operating at Reynolds number and swirl number equal to 30'000 and 0.61, respectively. Measurements are carried out via InfraRed Thermography using a heated thin foil as heat flux sensor, varying the impingement distance from 1 to 10 nozzle diameters. Numerical simulations of the same configurations are performed with a commercial software (Ansys Fluent) to test the capability of different Reynolds-Averaged Navier-Stokes (RANS) equations-based turbulence models in predicting the heat transfer rates from wall to the swirling impinging jets.

1. Introduction

Impinging jets provide an effective and flexible way to transfer energy or mass in industrial applications and the have been successfully applied in very different scenarios, such as heat treatment, cooling of electronic components, heating of optical surfaces for defogging, cooling of turbine component or critical machinery structure [1, 2]. Among the main drawbacks of conventional impinging jets is the non-uniform heat transfer distribution [3]. The superimposition of a tangential motion to a conventional jet is one of the most effective methods to obviate this issue and to increase the heat transfer rates. The azimuthal motion is usually given to the jet by different mechanisms, with the most common solutions being guided-blades [4], radial vanes [5], rotation of some solid parts of the device [6] and helical inserts in a cylindrical tube [7]. Previous studies have shown that the geometrical configuration of the swirl generator significantly determines the boundary exit condition of the jet, with a considerable influence on the development of the jet and ultimately on its heat transfer capabilities. This explains the contradictory results available in the literature on the heat transfer from swirling impinging jets, which have shown both a reduction [7] or an increase [8] of the average heat transfer in the comparison with conventional impinging jets. The reduction of the heat transfer is typically associated with the formation of a recirculation zone in the proximity of the jet centreline; on the other side, the heat transfer enhancement is ascribed to the improved flow mixing and the impingement of coherent vortical structures on the plate. The morphology of swirling imping jets is thoroughly described in the work of Huang and El-Genk [9], where six different regions in the flow field are detected.

Regardless of the swirl generation mechanism, the behaviour of an incompressible swirling jet flow is generally determined by two dimensionless numbers, namely the Reynolds number $Re = U_0 D / \nu$, with U_0 being a characteristic velocity scale (usually the average exit velocity or bulk velocity U_b), D the diameter of the exit nozzle and ν the fluid kinematic viscosity, and the swirl number $S = 2G_\theta / (G_x D)$, where G_x is the axial flux of the axial momentum and the G_θ is the axial flux of the angular momentum [10]. Four regimes are commonly distinguished in terms of the swirl number: non-swirling jets ($S = 0$), weakly swirling jets ($0 < S < 0.4$), moderate swirling jet ($0.4 < S < 0.6$) and strongly swirling jets ($S > 0.6$). In the case of a swirling impinging jet, the flow behaviour is also affected by the dimensionless nozzle-to-plate distance H/D . Apart from the above parameters, the heat transfer rate \dot{q} , generally expressed in terms of the Nusselt number $Nu = \dot{q} D / (k \Delta T)$ (with k being the fluid thermal conductivity and ΔT the temperature difference between the solid wall and the fluid at the nozzle exit), is also dependent on the Prandtl number Pr and the turbulence intensity I . In the existing literature, only few works feature correlations of the heat transfer from a wall to a swirling impinging jet (e.g., [5]). This is because both experimental and numerical investigations require significant efforts and time to sweep such a wide parameter space. In particular, on the numerical side, while the use of turbulence models based on the Reynolds-Averaged Navier-Stokes (RANS) equations has been proven adequate for conventional impinging jets [2], large discrepancies with experimental measurements have been found for the swirling counterparts [11]. On the other side, the more accurate DNS and LES approaches are prohibitive for the study of this phenomenon especially at high Reynolds and swirl numbers (which imply the occurrence of large gradients of the flow quantities and thus require burdensome computational resources). Indeed, comparative experimental and numerical studies are rare at the current stage of the research, and further validation of the turbulence models for swirling impinging jets is desirable. In this wake, the present work reports on a comparison between experimental measurements and numerical simulations of the heat transfer from swirling impinging jets at $Re = 30'000$ and $S = 0.61$. Results are presented for different values of the dimensionless nozzle-to-plate distance H/D . Experimental measurements are performed by means of the InfraRed Thermography (IRT) using a heated thin foil as heat flux sensor; the flow exit velocities are also measured by Stereoscopic Particle Image Velocimetry (SPIV). Ansys Fluent (version 20.5) is used for the numerical computations. Several available turbulence models (the SST $k-\omega$ model, the Reynolds stress model, the $k-\epsilon$ RNG model with different wall treatments and the Transition $k-k_L-\omega$ model) are applied to the present configurations and their results are comparatively assessed against the experimental ground-truth measurements. In the

following, firstly in Section 2 the experimental and numerical setups are presented; then, in Section 3 results are reported and critically discussed; finally, conclusions are drawn in Section 4.

2. Experimental and numerical arrangements

The experimental apparatus is sketched in Fig. 1. An air flow is generated by a centrifugal blower, piloted by a vector inverter, and connected to a plenum chamber upstream of the swirl generator. Before entering the plenum chamber, the flow is passed across a heat exchanger and a flow meter.

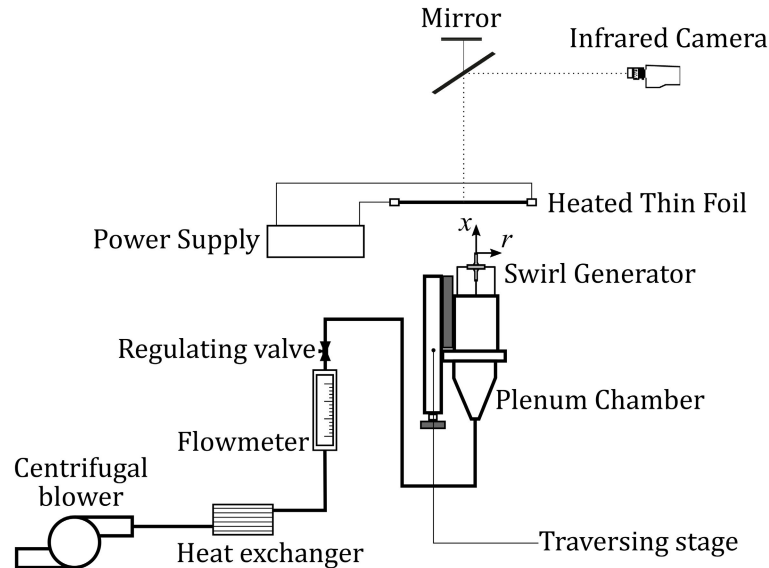


Fig. 1 Sketch of the experimental apparatus for the heat transfer measurements.

The swirl generator consists of three components (see Fig. 2):

- (inlet) a reinforced flat plate equipped with evenly spaced eight holes and a hose connector attached to;
- a disk provided with evenly spaced vanes: this is the component which actually generates the swirling motion;
- (outlet) the housing of the swirl generator which acts also as a nozzle.

The whole device is 3D-printed with standard resin. The three parts are specifically designed in order not to vary the passage area of the flow. Thus, the total passage areas of the vanes equal the cross-sectional circular areas of the inlet and the outlet nozzles, the diameter of which is $D = 10$ mm. Between the inlet and the outlet components, an O-Ring is employed to avoid air leakage. In the present experiments, the vane angle ϑ , shown in Fig. 2d, is set to 17.5° , which corresponds to a swirl number of $S = 0.61$ in the chosen experimental conditions.

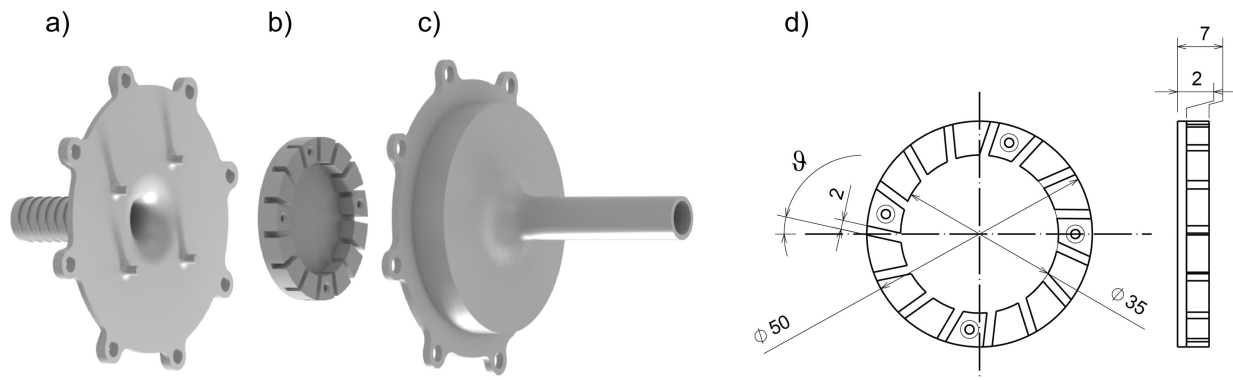


Fig. 2 Main components of the swirl generator: a) inlet; b) central body with radial vanes; c) outlet. d) Top view of the central body with vanes and definition of the vane angle.

The generated air swirling jet impinges normally onto a thin constantan foil (450 mm long, 200 mm wide, 50 μm thick), the flatness of which is ensured using a stiffening frame. The foil is steadily and uniformly heated by Joule effect and it is cooled by the swirling air jet impinging on it. The Joule heating is obtained by applying a steady voltage difference to the

edges of the foil, by using a stabilized DC power supply. The power supplied is measured with a multi-meter and is controlled by a rheostat. The separation of the nozzle exit section from the target plate is adjusted by using a precision translation stage with an accuracy of 0.1 mm:

The temperature of the foil is measured by an IR camera. This camera measures the temperature of the foil side opposite to that impinged by the swirling jet. This is acceptable because the Biot number ($Bi = hs/k$ where h is the convective heat transfer coefficient and s is the foil thickness the foil) is much smaller than 1, in such a way that the temperature can be considered uniform across the foil thickness with good approximation. The back side of the foil (i.e., the one opposite to the impingement) is coated with the high emissivity paint ($\varepsilon = 0.95$) in order to increase the signal-to noise ratio. The spatial resolution of the camera is 4.6 pixel/mm (46 pixel/D). The IR camera is calibrated with a black body for the whole measurement range taking also into account the mirror presence in the optical path.

By applying the steady state energy balance to the foil, the convective heat transfer coefficient h can be evaluated as [11]:

$$h = \frac{\dot{q}_J - \dot{q}_r - \dot{q}_k - \dot{q}_n}{T_w - T_{aw}} \quad (1)$$

where:

- \dot{q}_J is the heat Joule flux (computed by measuring both voltage and current across the foil);
- T_w and T_{aw} are the wall and the adiabatic wall temperature, respectively;
- $\dot{q}_r = \varepsilon\sigma(T_w^2 - T_a^2)$ is the radiation heat flux, with σ being the Stefan-Boltzmann's constant and T_a the ambient temperature (measured during the experiment);
- $\dot{q}_k = \lambda_f s \nabla_{xy}^2 T_w$ is the loss for tangential conduction in the foil, with λ_f being the foil thermal conductivity and $\nabla_{xy}^2(\cdot)$ the 2D Laplacian operator;
- \dot{q}_n the natural convection flux (computed using semi-empirical correlation [12]).

The temperatures T_w and T_{aw} are measured in two separate tests, respectively the “hot test”, with the electric current on, and the “cold test”, with the electric current off. For each run, 1600 thermal images are recorded at a frame rate of 50 Hz and subsequently averaged. The uncertainties in the determination of the time-averaged local Nusselt numbers are estimated by the Moffat's method. This method is based on the propagating the uncertainties of all the measured quantities involved in the computation of the Nu to determine their contribution to the uncertainty of Nu itself. The overall uncertainty is then calculated as the square root of the sum of the squares. Typical values of the estimated measurement uncertainty are around 10% (of the measured quantities).

A sketch of the computational domain and the corresponding boundary conditions employed for the simulations is shown in Fig. 3. A considerable simplification is obtained by treating the problem as axisymmetric, as also done in previous works (e.g., [5, 10]). This is possible since the time-averaged flow field is resolved by integrating the RANS equations. As a consequence, the computational domain is a rectangle extending over one of the meridional planes passing through the jet axis. The lower boundary of the domain is placed at the distance x_{PIV} from the nozzle exit at which the velocity measurements are performed by means of SPIV, whereas the upper boundary coincides with the wall. Therefore, the height of the domain is equal to $H - x_{PIV}$. Along the radial direction, the leftmost edge of the domain is the jet axis, whereas the rightmost edge is arbitrarily located at a radial distance equal to L . In the present numerical tests $L = 10D$. At the lower edge of the domain ($x = x_{PIV}$), a velocity inlet boundary conditions is imposed for $r \leq 2D$, while the pressure outlet condition is applied for $2D < r \leq 10D$. At the upper edge ($x = H$), a wall-type boundary condition is imposed, with no-slip condition for velocity and prescribed heat flux for energy (equal to the measured \dot{q}_J of the experiments). At the jet-axis, an symmetry boundary condition is applied, while the edge $r = L$ is considered as a pressure outlet surface.

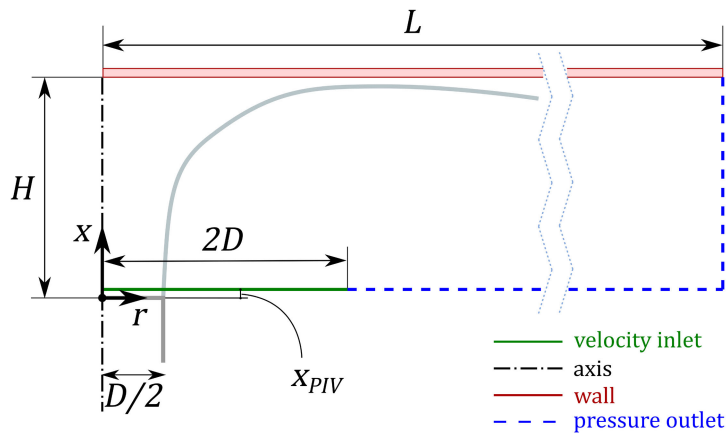


Fig. 3 Schematic of the computational domain and boundary condition used for the simulations.

As aforementioned, the velocity inlet boundary condition is assigned based on a set of SPIV measurements performed in the same operating conditions of the heat flux measurements ($Re = 30'000$ and $S = 0.61$). The details about the velocimetry experimental apparatus are not reported here for conciseness. Measurements are carried out in a plane orthogonal to the jet axis and located at $x_{PIV} = 0.05D$ (to reduce laser light reflections on the nozzle exit section). The velocity and turbulence profiles have been determined in the presence of a transparent wall placed at a distance $H = 2D$ from the nozzle exit. The results are reported in Fig. 4. It is interesting to note how the radial component of the exit velocity, although considerably smaller than the remaining components, is not zero; specifically, it is positive over the exit section area due to the centrifugal forces related to the swirl and negative outside of it due to the jet entrainment. The presence of a minimum of the axial velocity at the jet axis indicates the occurrence of vortex breakdown [4], although no reverse flow is indeed observed in the present case. Relatedly, turbulent fluctuations (i.e., the turbulent kinetic energy k) are larger in the proximity of the jet axis, i.e., in the region of recirculation (where the most chaotic behaviour is expected). Depending on the turbulence model adopted for the simulation, the flow velocity and k are not the only quantities to be assigned at the velocity inlet. The energy dissipation rate ε and the specific energy dissipation rate ω are also required for the k - ε and the k - ω models. These quantities are calculated from k using the following relationships [5]:

$$\varepsilon = \frac{C_{\mu}^{3/4} k^{3/2}}{l} \quad (2)$$

$$\omega = \frac{k^{1/2}}{C_{\mu}^{3/4} l} \quad (3)$$

Where C_{μ} is a model constant ($= 0.09$ for the k - ε model and 0.085 for the k - ω model) and l a turbulent length scale, assumed to be equal to $0.07D$.

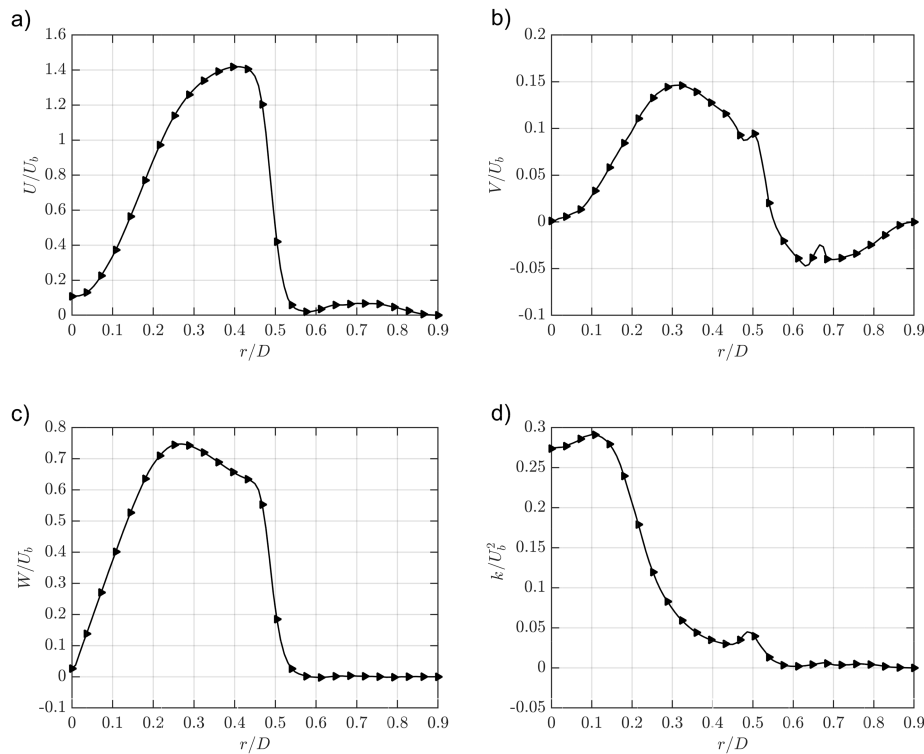


Fig. 4 Velocity inlet conditions for the numerical simulations. Profiles of the a) axial (U), b) radial (V), c) swirling (W) velocities and d) the turbulent kinetic energy (k) measured by SPIV at $x/D = 0.05$ for $Re = 30'000$ and $S = 0.61$.

As concerns the computational grid, a grid refinement study has been performed to assess the independence of the results from the selected mesh resolution. Specifically, three different meshes, denoted as fine, medium and coarse, consisting of 166'980, 74'140 and 14'934 nodes, have been considered. These meshes are designed with similar criteria and are characterized by a finer resolution in proximity of the jet axis and the wall, where the most severe gradients of the thermo-fluid dynamic properties are expected. Fig. 5 reports the results from the simulations performed using the k - ε RNG model with enhanced wall treatment at $Re = 30'000$, $S = 0.61$ and $H/D = 2$ for the three considered grids. It is shown that the discrepancies between the medium and the fine cases are negligible except in the region close to the jet axis. For this reason, all the results presented in the following section are related to the medium mesh.

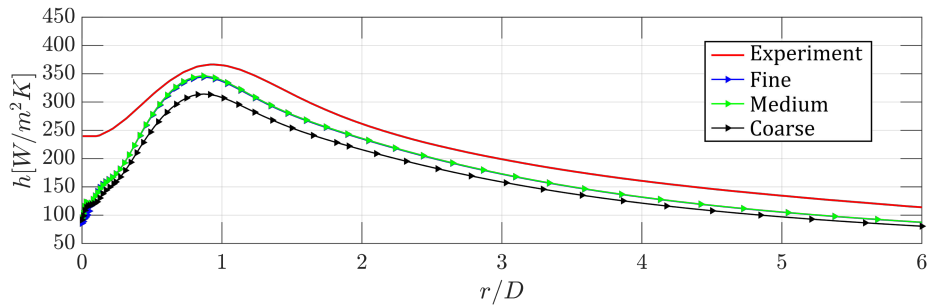


Fig. 5 Results from mesh refinement study. Radial distribution of the convective heat transfer coefficient from simulations performed using the $k-\varepsilon$ RNG model with enhanced wall treatment at $Re = 30'000$, $S = 0.61$ and $H/D = 2$ for three different grids: fine (166'980 nodes), medium (74'140 nodes) and coarse (14'934 nodes). Experimental measurements (azimuthally averaged) are also reported for comparison.

Finally, as regards the numerical scheme, a pressure-based formulation with the COUPLED scheme for pressure-velocity coupling and the second order upwind method is used for the spatial discretization of convective terms in the governing equations, while the second order PRESTO scheme is used for pressure interpolation. The local criterion for numerical convergence has been set to 10^{-6} for all the equations solved.

3. Results

The maps of the Nusselt number measured experimentally are presented in Fig. 6 and Fig. 7. At small impingement distances, the heat transfer distribution exhibits a ring-shaped region of maximum values which is associated with the presence of a recirculation zone in proximity of the jet axis. A minimum on the jet centreline is observed up to $H/D = 6$, while for larger impingement distances a bell-shaped distribution is found. The maps in Fig. 6 and Fig. 7 confirm that the flow field from swirling impinging jets is axisymmetric on the time average, since deviations from axisymmetry are negligible in the Nu distribution. (and consistent with misalignment and imperfections of the experimental setup).

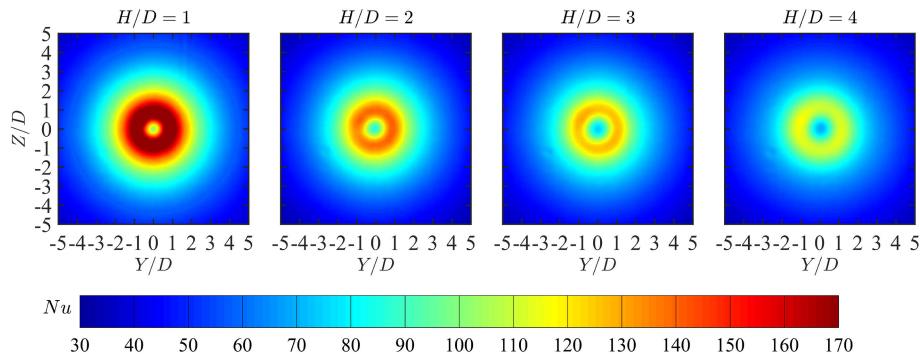


Fig. 6 Maps of the Nusselt number for small impingement distances. $Re = 30'000$, $S = 0.61$.

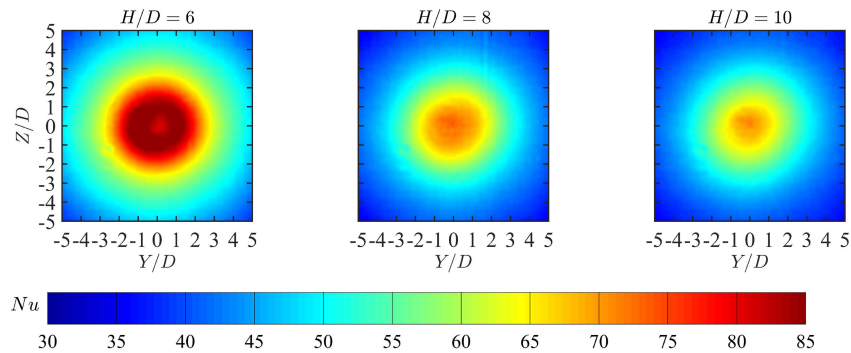


Fig. 7 Maps of the Nusselt number for large impingement distances. $Re = 30'000$, $S = 0.61$.

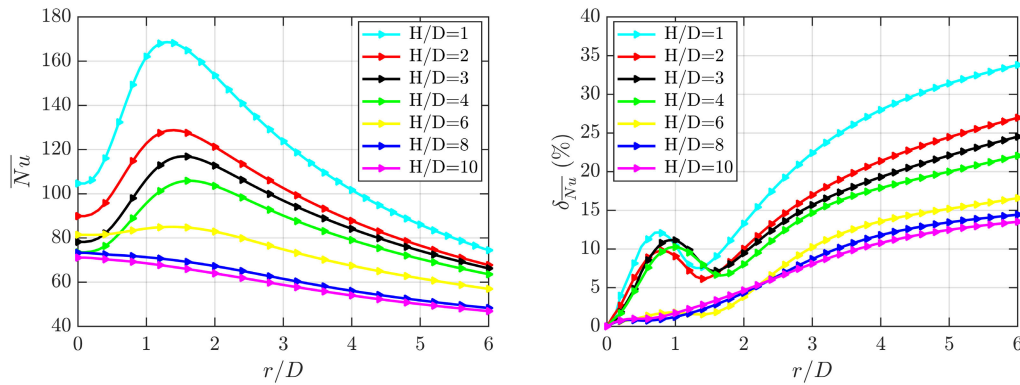


Fig. 8 Profiles of area-averaged Nusselt number \overline{Nu} (left) and non-uniformity parameter $\delta_{\overline{Nu}}$ (right) as a function of the radius r of the averaging area for different impingement distances. $Re = 30'000$, $S = 0.61$.

Fig. 8 reports the profiles of area-averaged Nusselt number \overline{Nu} and non-uniformity parameter $\delta_{\overline{Nu}}$ as a function of the radius r of the averaging area for all the investigated impingement distances. The reader is referred to [13] for the definition of such quantities. From this figure, it is clear that the heat transfer rates are monotonically decreasing with the impingement distance at least for $r/D \geq 0.5$. The radius of the circular area corresponding to the averaged maximum cooling rate slightly increases from $\approx 1.1D$ to $\approx 1.5D$ as H/D varies between 1 and 4. At $H/D = 6$ no evident peak is found in the $\overline{Nu}(r)$ profile, while for greater impingement distances a monotonic behaviour is found. The right plot shows that the disappearance of a peak is accompanied by better values of the heat transfer uniformity. It is therefore possible to conclude that the presence of a recirculation zone has a negative effect in terms of the heat transfer distribution.

The different RANS-based turbulent models available in Ansys Fluent are tested in two of the above investigated configurations, namely $H/D = 2$, which is representative of the condition in which a recirculation zone forms on the impingement plate with the subsequent generation of a ring-shaped region of high Nu values in the heat transfer map, and $H/D = 8$, which is representative of the condition in which no recirculation zone is formed at the impingement, thus leading to a bell-shaped Nu distribution. The comparative assessment of such models against the experimental measurements are reported in Fig. 9.

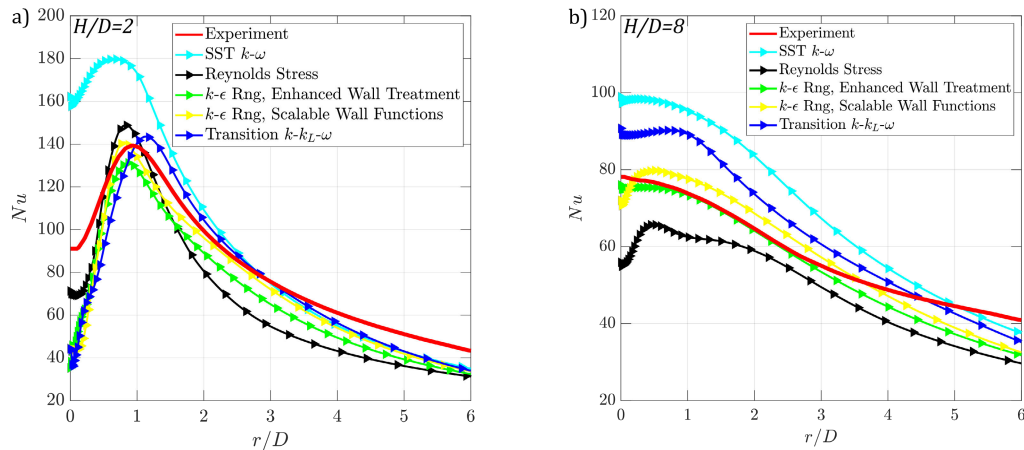


Fig. 9 Comparison between experimental measurement of Nu profile as a function of the radial distance r and computations from numerical simulations performed with different turbulence models at $Re = 30'000$, $S = 0.61$ and a) $H/D = 2$ and b) $H/D = 8$.

With regard to the case $H/D = 2$ (Fig. 9a), all the investigated turbulence models predict a region of lower heat transfer rates in the proximity of the jet axis, a subsequent ring-shaped region of maximum Nu and a monotonically decreasing behaviour further downstream. In principle, this trend resembles that observed experimentally; however, noticeable differences are found between the experiment and the simulations and no turbulence model offers a fully satisfying prediction. Indeed, the values of Nu in the centre of impingement are largely underestimated by all the models, except for the SST $k-\omega$ model, which largely overrates them. This suggests that the flow structure of the recirculation zone is not faithfully reproduced in any case. Also the position of the peak (ring-shaped region) is not correctly captured by any of the models, although the $k-\epsilon$ RNG model with scalable wall functions reproduces its value with good accuracy. The misplaced position of the peak indicates an erroneous prediction of the width of the recirculation zone and the jet spreading rate. In the region of the monotonic decrease of Nu , the Transition $k-k_L-\omega$ model behaves better than the others in the comparison with experimental measurements. Nevertheless, for $r/D > 3$ all the turbulence models exhibit a decrease of

Nu at a faster rate than the experimentally measured curve; this might be related to a faster growth of the thermal boundary layer in the numerical case.

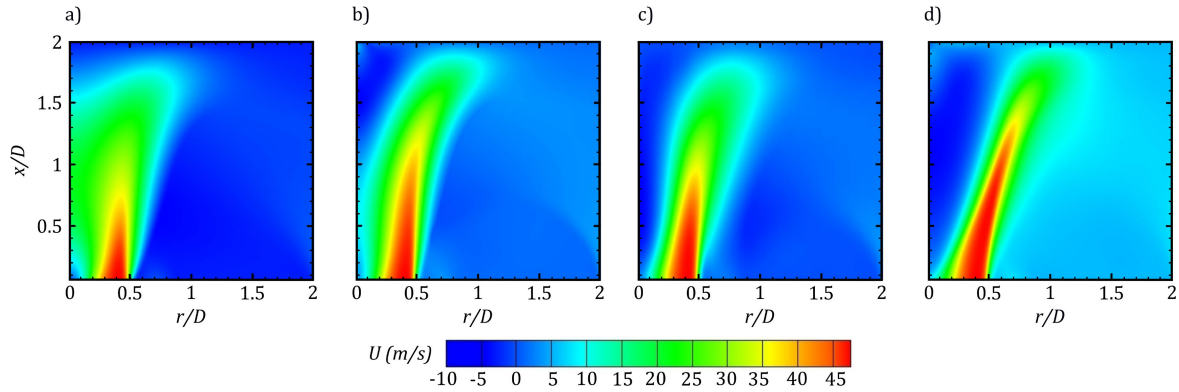


Fig. 10 Maps of axial velocity for $H/D = 2$ from numerical simulations performed using: a) the SST $k-\omega$ model; b) the Reynolds stress model; c) the $k-\epsilon$ RNG model with enhanced wall treatment; d) the Transition $k-k_L-\omega$ model. $Re = 30'000$, $S = 0.61$.

In order to relate the behaviours shown in Fig. 9a to the predicted structure of the swirling impinging flow field, in Fig. 10 the maps of the axial velocity obtained from four of the investigated turbulence models are presented. From this figure, it is evident that the high values of Nu achieved by the SST $k-\omega$ model (Fig. 10a) are ascribable to the small extent of the recirculation zone and the subsequent high momentum of the flow at the impingement in the proximity of the jet axis. Moreover, it is possible to see that the location of the peak in the Nu profile is correlated to the width of the recirculation zone and the jet spreading rate: in fact, the Transition $k-k_L-\omega$ model (Fig. 10d), which shows the most forward location of such a peak, features also the wider recirculation zone and the faster jet spreading rate.

With regard to the case $H/D = 8$ (Fig. 9b), it is interesting to note that only the SST $k-\omega$ model and the $k-\epsilon$ RNG model with enhanced wall treatment show a bell-shaped distribution of the Nusselt number as that observed experimentally. The Reynolds stress model and the $k-\epsilon$ RNG model with scalable wall functions present a minimum on the jet axis, whereas the Transition $k-k_L-\omega$ model exhibits a plateau over the range $r/D \leq 1$. Both the SST $k-\omega$ model and the Transition $k-k_L-\omega$ model greatly overestimates the heat transfer rates in the region around the jet axis; on the other side, the $k-\epsilon$ RNG model with enhanced wall treatment matches the experimental measurements with excellent accuracy for $r/D \leq 3$. As for $H/D = 2$, downstream of $r/D = 3$, the numerical models predict a faster decrease of Nu as r increases.

The above analysis suggests that for low impingement distances the Transition $k-k_L-\omega$ model offers the best performance, whereas for high impingement distances the $k-\epsilon$ RNG model with enhanced wall treatment greatly outperforms the other models in the comparison with the experimental measurements. In order to further validate this observation, numerical simulations with both these two models have been performed for the other values of H/D investigated experimentally. The corresponding results are reported in Fig. 11. These diagrams confirm that the Transition $k-k_L-\omega$ model works efficiently for $H/D = 3$ (Fig. 11a) over the range $0 < r/D < 3$, whereas, outside of this region, it underestimates the experimental values. On the other side, the $k-\epsilon$ RNG model with enhanced wall treatment shows lower values than the experimental measurements for any r . Conversely, at $H/D = 10$ (Fig. 11c), the Transition $k-k_L-\omega$ model is found to overrate the experimental measurements, while a nice agreement is observed for the $k-\epsilon$ RNG model in the region $r/D < 3$. However, at intermediate impingement distances (Fig. 11b), both the models offer unsatisfying prediction of the experimentally observed behaviour.

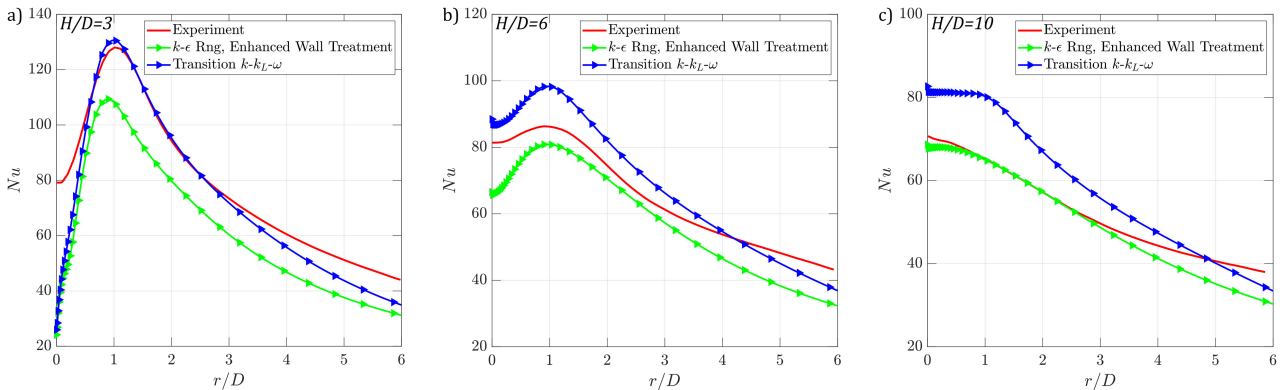


Fig. 11 Comparison between experimental measurement of Nu profile as a function of the radial distance r and computations from numerical simulations performed with the $k-\epsilon$ RNG model with enhanced wall treatment and the Transition $k-k_L-\omega$ model at $Re = 30'000$, $S = 0.61$ and a) $H/D = 3$, b) $H/D = 6$ and c) $H/D = 10$.

4. Conclusions

The present work has reported on a comparative experimental and numerical study of the heat transfer from a heated wall to a swirling impinging jet operating at Reynolds and swirl numbers respectively equal to 30'000 and 0.61. Measurements are performed via InfraRed Thermography using a heated thin foil as heat flux sensor. Several configurations are investigated by varying the impingement distance of the jet from 1 to 10 nozzle diameters. The same configurations have been tested numerically via a commercial numerical software (Ansys Fluent), by applying different turbulence models based on the RANS equations, namely the SST $k-\omega$ model, the Reynolds stress model, the $k-\varepsilon$ RNG model with different wall treatments and the Transition $k-k_L-\omega$ model. In the literature, the SST $k-\omega$ model has been proven to accurately predict the thermal behaviour of conventional impinging jets [2], thus, more recently it has been applied also to investigate the heat transfer capabilities of swirling jets and develop correlation for Nu as a function of Re, S and H/D [5]. Conversely, our results show that this model is inaccurate for any value of H/D in the present flow conditions and, specifically, it greatly overestimates the experimental measurements. Moreover, among those under inspection, no model behaves accurately with varying H/D . At small impingement distances, the Transition $k-k_L-\omega$ model provides the best predictions, although the heat transfer rate are underestimated in the proximity of the jet axis. This flaw is common to all the investigated turbulence models and suggest that the flow structure of the recirculation zone forming at small impingement distances is not correctly captured. For larger impingement distances, the $k-\varepsilon$ RNG model with enhanced wall treatment outperforms the remaining models. However, for all the investigated H/D , the numerical solutions obtained by the different models envisage a faster decrease of the heat transfer rate for $r/D = 3$ than the experimental measurements, which might be related to an incorrect prediction of the growth of the thermal boundary layer thickness as the flow develops along the wall.

REFERENCES

- [1] Martin H., "Heat and Mass Transfer between Impinging Gas Jets and Solid Surfaces". Advances in Heat Transfer, vol. 13, pp. 1-60, Academic Press, New York, 1977.
- [2] Zuckerman, N., Lior N. "Jet impingement heat transfer: physics, correlations, and numerical modeling." Advances in Heat Transfer, vol. 39, pp. 565-631, 2006.
- [3] Carlomagno, G.M., Ianiro, A. "Thermo-fluid-dynamics of submerged jets impinging at short nozzle-to-plate distance: a review." Experimental Thermal and Fluid Science, vol. 58, pp. 15-35, 2014.
- [4] Harvey, J. K. "Some observations of the vortex breakdown phenomenon." Journal of Fluid Mechanics, vol. 14, no. 4, pp. 585-592, 1962.
- [5] Ortega-Casanova, J. "CFD and correlations of the heat transfer from a wall at constant temperature to an impinging swirling jet." International Journal of Heat and Mass Transfer vol. 55, no. 21-22, pp. 5836-5845, 2012.
- [6] Escudier, M. P., Bornstein, J., Zehnder, N. "Observations and LDA measurements of confined turbulent vortex flow." Journal of Fluid Mechanics, vol. 98, no. 1, pp. 49-63, 1980.
- [7] Ianiro, A., Cardone, G.. "Heat transfer rate and uniformity in multichannel swirling impinging jets." Applied Thermal Engineering, vol. 49, pp. 89-98, 2012.
- [8] Wen, M.-Y., Jang, K.-J.. "An impingement cooling on a flat surface by using circular jet with longitudinal swirling strips." International Journal of Heat and Mass Transfer, vol. 46, no. 24 pp. 4657-4667, 2003.
- [9] Huang, L., El-Genk, M.-S.. "Heat transfer and flow visualization experiments of swirling, multi-channel, and conventional impinging jets." International Journal of Heat and Mass Transfer, vol. 41, no. 3, pp. 583-600, 1998.
- [10] Ahmed, Z. U., Al-Abdeli, Y.-M., Guzzomi, F. G.. "Flow field and thermal behaviour in swirling and non-swirling turbulent impinging jets." International Journal of Thermal Sciences, vol. 114, pp. 241-256, 2017.
- [11] Astarita, T., Carlomagno, G: M. *Infrared thermography for thermo-fluid-dynamics*. Springer Science & Business Media, 2012.
- [12] Welty, J., Rorrer, G.L., Foster, D. G.. *Fundamentals of momentum, heat, and mass transfer*. John Wiley & Sons, 2020.
- [13] Paolillo, G., Greco, C.S., Cardone, G. "Impingement heat transfer of quadruple synthetic jets." International Journal of Heat and Mass Transfer, vol. 135, pp. 1192-1206, 2019.